ADVANCED FUNCTIONAL MATERIALS
www.afm-journal.de

Surface Reconstruction of Co-based Catalysts for Enhanced Oxygen Evolution Activity in Anion Exchange Membrane Water Electrolysis

*Sanghwi Han, Jungwon Park, and Jeyong Yoon**

Developing high-performance and durable electrocatalysts for the oxygen evolution reaction (OER) is of utmost importance for green hydrogen production via anion exchange membrane water electrolysis (AEMWE). Herein, it is presented that a straightforward surface reconstruction strategy for preparing a robust Co-based OER catalyst with increased mass transfer activity while preserving the active CoOOH phase during the OER. This strategy comprises electrochemical oxidation of electrodeposited Co-based catalysts prior to heat treatment, allowing for the meticulous control of the oxidation potential to optimize the OER activity. The optimized catalyst exhibits an overpotential of 190 mV at 10 mA cm^{-2} and a Tafel slope of 32.7 mV dec^{-1} under half-cell conditions. In an AEMWE single-cell system, it shows a current density of 1590 mA cm^{-2} at 1.8 V and 60 °C and demonstrates a degradation rate of 0.2 mV h^{-1} during 1000 h of operation at 500 mA cm^{-2}. This study not only provides a simple yet potent strategy to enhance the OER activity but also offers insights regarding the factors enhancing the OER performance.

1. Introduction

Anion exchange membrane water electrolysis (AEMWE) has emerged as a promising technology toward the implementation of the oncoming hydrogen economy.[1–10] AEMWE systems are strategically formulated to integrate the advantages of alkaline water electrolysis, in which cost-effective transition metal–based catalysts are used under alkaline conditions, and proton exchange membrane water electrolysis, which incorporates zero-gap configurations and nonporous membranes, to enhance the hydrogen production efficiency.[11–17] However, the technological potential of AEMWE is limited by the sluggish kinetics of the oxygen evolution reaction (OER); therefore, the development of high-performance and durable OER catalysts is essential.[1,5,18–25]

Among the transition metal–based OER catalysts, Co-based catalysts have attracted substantial interest owing to their high OER performance, cost-effectiveness, and structural versatility.[26–33] Although numerous structures have been reported, most Co-based catalysts undergo phase transitions depending on the electrochemical potential, primarily exhibiting the CoOOH or CoO_2 phase during the OER.[26,32,34,35] Among them, the CoOOH phase is a key active site for the OER due to its rapid kinetics.[28,29,31,34–36] Moreover, the presence of Co(IV) = O species induces substantial delays in the OER kinetics compared with CoOOH species.[37] Hence, preserving the CoOOH phase during the OER via surface reconstruction is highly desirable. Despite considerable research in this regard,[34,38–40] comprehensive investigations on the factors influencing surface reconstruction are still lacking. Moreover, developing a straightforward and universal methodology for an effective and applicable surface reconstruction is imperative.

Achieving efficient electrolysis at industrial-scale high current densities (>500 mA cm^{-2}) in AEMWE systems requires catalysts with excellent mass transfer activity. The mass transfer activity of catalysts can be enhanced by increasing the number of active sites, establishing a porous structure, and minimizing the catalyst thickness.[41,42] Accordingly, surface reconstruction strategies that optimize the mass transfer activity while preserving the CoOOH phase are required to realize practical water electrolysis. Moreover, considering that the majority of AEMWEs have exhibited poor performance (<1500 mA cm^{-2} at 1.8 V) and durability (<100 h),[9,42–49] a catalyst with exceptional activity and durability is urgently needed.

S. Han, J. Park, J. Yoon
School of Chemical and Biological Engineering
Institute of Chemical Processes
Seoul National University (SNU)
Seoul 08826, Republic of Korea
E-mail: jeyong@snu.ac.kr
J. Park
Center for Nanoparticle Research
Institute for Basic Science (IBS)
Seoul 08826, Republic of Korea
J. Park
Institute of Engineering Research
College of Engineering
Seoul National University
Seoul 08826, Republic of Korea
J. Park
Advanced Institute of Convergence Technology
Seoul National University
Suwon-si, Gyeonggi-do 16229, Republic of Korea

The ORCID identification number(s) for the author(s) of this article can be found under https://doi.org/10.1002/adfm.202314573

DOI: 10.1002/adfm.202314573

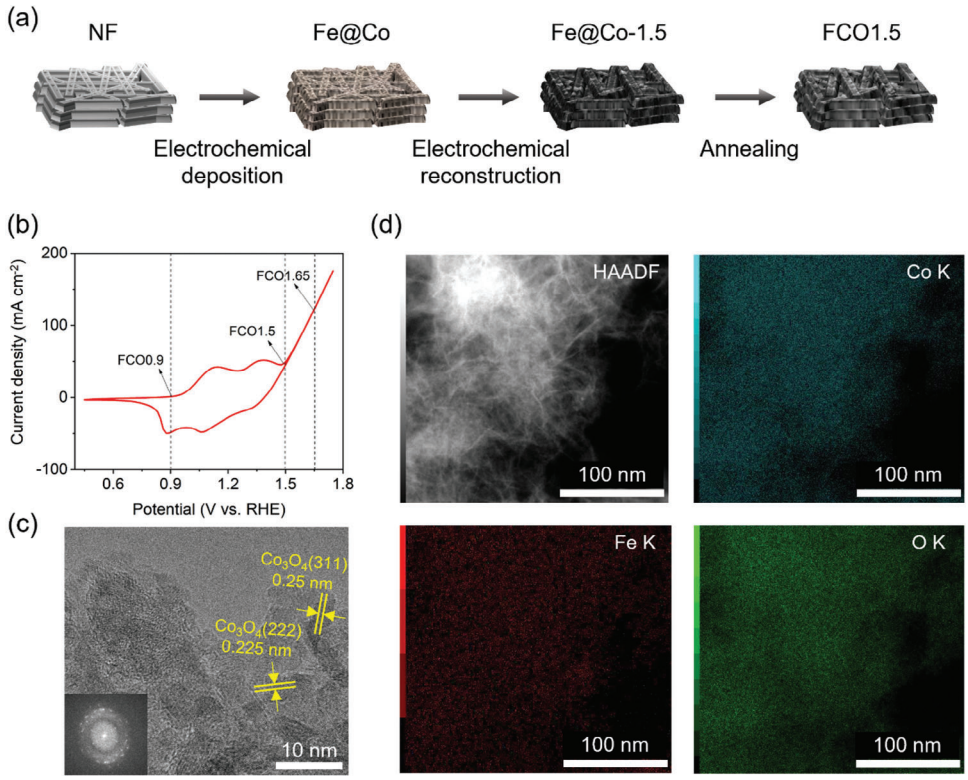

Figure 1. Fabrication and characterization of the Co-based catalysts. a) Schematic of the synthesis of the FCO1.5 electrode. b) CV result of the Fe@Co electrode in a 1 M KOH solution using a scan rate of 50 mV s^{-1} without iR-compensation. c) TEM image and d) TEM–EDS elemental mapping of the FCO1.5 catalyst.

Herein, we developed a high-performance and durable Co-based OER catalyst using a simple and scalable surface reconstruction strategy comprising electrochemical reconstruction and subsequent heat treatment. Building upon our previous research, a sequentially electrodeposited Co-based catalyst (Fe@Co) was employed as a model catalyst,[3] which was subjected to heat treatment to improve its durability. The implementation of electrochemical reconstruction before the heat treatment was proven to enhance the OER activity. In particular, subjecting the catalyst to a certain potential before heat treatment allowed preserving the CoOOH phase during the OER and increasing the number of active sites and porosity. The optimized catalyst exhibited an overpotential of 190 mV at 10 mA cm^{-2} and a Tafel slope of 32.7 mV dec^{-1} under half-cell conditions. In an AEMWE single-cell system, it exhibited a current density of 1590 mA cm^{-2} at a cell voltage of 1.8 V and 60 °C and a degradation rate of 0.2 mV h^{-1} after 1000 h of operation at 500 mA cm^{-2}. These findings validate the efficacy of the developed strategy, which can be expected to contribute substantially to the development of OER catalysts for AEMWE systems owing to its simplicity and scalability.

2. Results and Discussion

2.1. Preparation and Characterization of the Co-Based Electrodes

Figure 1 shows a schematic of the strategy for the catalyst synthesis and the structural characteristics of the synthesized electrodes. As shown in Figure 1a, the catalyst was fabricated via a three-step strategy. Initially, a bare Ni felt (NF) was subjected to sequential electrodeposition of Fe and Co, resulting in the formation of a Fe@Co catalyst with an amorphous $Co(OH)_2$ phase on the surface.[3] Subsequently, the catalyst was subjected to electrochemical reconstruction by controlling the applied potential, followed by heat treatment. The electroplated catalysts and heat-treated catalysts were denoted as Fe@Co-X and FCOX (FCO stands for FeCo-based oxidized catalyst), respectively, with X representing the applied potential during the electrochemical reconstruction process. An electrode subjected to heat treatment but not to an electrochemical process was also prepared and denoted as FC. Figure 1b shows a cyclic voltammetry (CV) plot of the Fe@Co electrode. The peaks observed at ≈1.1 and 1.3 V (versus the reversible hydrogen electrode (RHE)) present the oxidation peaks of Co^{2+}/Co^{3+} and Co^{3+}/Co^{4+}, respectively,[26,36,50] indicating that the surface of Fe@Co mainly retains the $Co(OH)_2$ phase at <0.9 V and maintains the Co^{3+} or Co^{4+} phase at >1.5 V (versus RHE). Accordingly, comparison groups were established at potentials of 0.9 V (pre-Co oxidation), 1.5 V (post-Co oxidation), and 1.65 V (versus RHE) (post-OER). The synthesized catalysts contained ≈380 μg cm^{-2} of Co and approximately one-sixth of that amount of Fe, as confirmed via inductively coupled plasma mass spectrometry (ICP-MS) analysis (Table S1, Supporting Information). X-ray diffraction (XRD) measurements were performed to analyze the crystal structures of the catalysts (Figure S1, Supporting Information). However, because the peaks of the NF substrate were so large, the peak of the catalyst could not be observed. The

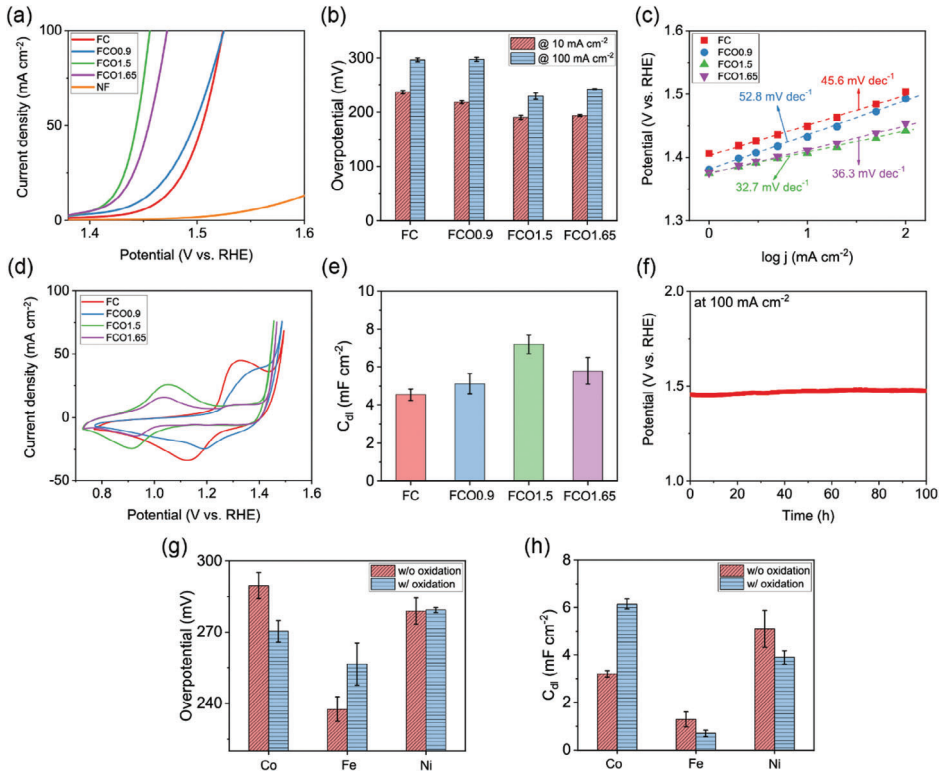

Figure 2. Electrocatalytic activity and properties of the FC-catalyst series under half-cell conditions. a) LSV curves of the as-prepared electrodes in 1 M KOH. b) Comparison of the overpotentials required for 10 and 100 mA cm^{-2}. Comparison of c) Tafel slopes, d) CV results (scan rate: 50 mV s^{-1}), and e) C_{dl} values of the FC-catalyst series. f) Durability test of FCO1.5 at 100 mA cm^{-2} for 100 h. Comparison of g) overpotentials at 10 mA cm^{-2} and h) C_{dl} values for Co, Fe, and Ni electrodes with (w/ oxidation) and without (w/o oxidation) electrochemical oxidation prior to heat treatment.

presence of a Co_3O_4 structure was confirmed via the transmission electron microscopy (TEM) image of FCO1.5 (Figure 1c). Moreover, the TEM–energy-dispersive spectroscopy (EDS) mapping of the FCO1.5 catalyst revealed a homogeneous distribution of Co and O as the main elements (Table S2, Supporting Information; Figure 1d).

2.2. Electrochemical Properties of the Co-Based Electrodes

A comparison of the electrochemical catalytic properties of the synthesized catalysts in a 1 M KOH solution under half-cell conditions is presented in **Figure 2**. The linear sweep voltammetry (LSV) curves show that FCO1.5 exhibited the highest OER performance with the lowest overpotential of 190 mV at 10 mA cm^{-2} among the prepared electrodes (Figure 2a). At 10 mA cm^{-2}, FC, FCO0.9, FCO1.5, and FCO1.65 exhibited overpotentials of 237, 219, 190, and 194 mV, respectively (Figure 2b). At 100 mA cm^{-2}, the overpotential differences became more pronounced, with overpotentials of 297, 298, 230, and 242 mV for FC, FCO0.9, FCO1.5, and FCO1.65, respectively. This result implies that the electrochemical reconstruction before heat treatment substantially affects the OER performance of the Co-based catalysts, with an optimal point. To further investigate the OER kinetics, the Tafel slopes were compared (Figure 2c). The steady-state potential at each current density was determined for accurate Tafel slope plotting. FCO1.5 and FCO1.65 exhibited lower Tafel slopes (32.7 and 36.3 mV dec^{-1}, respectively) than FC (45.6 mV dec^{-1}), implying accelerated kinetics or potential variance in the OER mechanism.[51] Conversely, FCO0.9 exhibited a slope of 52.8 mV dec^{-1}, surpassing that of FC. Figure 2d displays the CV results of the electrodes, revealing the Co redox characteristics. Notably, FCO1.5 and FCO1.65 predominantly displayed oxidation peaks at approximately 1.1 V associated with Co^{2+}/Co^{3+}, whereas FC and FCO0.9 exhibited oxidation peaks at ≈1.3 V (versus RHE) corresponding to Co^{3+}/Co^{4+}. This implies the prevalence of the Co^{4+} phase under OER conditions in FC and FCO0.9, whereas FCO1.5 and FCO1.65 exhibited a dominance of Co^{3+}, a trend will be further corroborated by the material analyses. This phase difference can influence both the extrinsic and intrinsic catalytic performance; thus, the electrochemically active surface area (ECSA) was determined by measuring the double-layer capacitance (C_{dl}) within the non-Faradaic potential range (Figure S2, Supporting Information) and the intrinsic performance of the electrodes was compared. FCO1.5 exhibited a C_{dl} value of 7.2 mF cm^{-2}, which was ≈1.6 times greater than that of FC (4.6 mF cm^{-2}), while the remaining catalysts showed C_{dl} values similar to that of FC (Figure 2e). The ECSA-normalized LSV curves indicate the superior intrinsic activity of FCO1.5 among the electrodes (Figure S3a, Supporting Information). At an overpotential of 250 mV, FCO1.5 exhibited a specific activity of 1.4 mA cm^{-2} and mass activity of 678 A g^{-1}, which were 8-fold and 13-fold higher than those of FC (0.17 mA cm^{-2} and 51 A g^{-1}, respectively) (Figure S3b, Supporting Information). In addition to activity, stability is also an

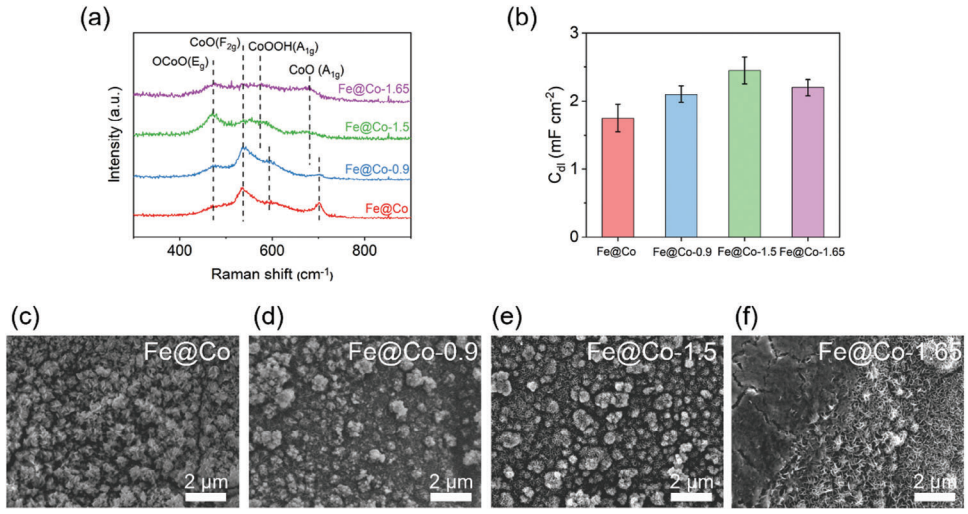

Figure 3. Material and electrochemical characteristics of the Fe@Co-electrode series. a) Raman spectra and b) C_{dl} values of the Fe@Co-electrode series. SEM images of the c) Fe@Co, d) Fe@Co-0.9, e) Fe@Co-1.5, and f) Fe@Co-1.65 electrodes.

essential feature for electrocatalysts. FCO1.5 displayed excellent durability for 100 h of operation at 100 mA cm^{-2} (Figure 2f), with no discernible changes in the LSV curves and no structural changes detected via Raman spectroscopy, scanning electron microscopy (SEM) and XRD analyses (Figure S4, Supporting Information). These results confirm that the OER performance of the Co-based catalysts can be modulated by controlling the electrochemical surface reconstruction, enabling the development of high-performance and durable OER catalysts.

To decouple the surface reconstruction effect of Co from that of Fe and Ni, single-electroplated Co, Fe, and Ni catalysts were compared (see details in the experimental section). Each electrode was prepared using two approaches: one involved electrochemical oxidation at 1.5 V (versus RHE) followed by heat treatment (w/ oxidation) and the other involved heat treatment without oxidation (w/o oxidation). The CV results for the Co, Fe, and Ni electrodes affirmed that the oxidation peaks of all three catalysts appeared below 1.5 V (versus RHE), thus validating the suitability of this specified threshold (Figure S5, Supporting Information). Interestingly, the overpotential of the Co catalyst at 10 mA cm^{-2} decreased by ≈19 mV through the implementation of the oxidation process, whereas that of the Fe and Ni catalysts increased by ≈19 and 1 mV, respectively (Figure 2g; Figure S6, Supporting Information). Furthermore, the oxidation process resulted in a two-fold increase in the C_{dl} value of the Co electrode, whereas it caused a slight reduction in the C_{dl} values of the Fe and Ni electrodes (Figure 2h; Figure S7, Supporting Information). These results demonstrate that the enhancement of the OER performance and the increase in ECSA via electrochemical reconstruction before heat treatment were mainly associated with Co.

2.3. Characteristics of the Co-Based Catalysts Before Heat Treatment

To investigate the effect of electrochemical reconstruction on the Co-based catalysts, the material and electrochemical properties of the catalysts subjected to electrochemical treatment without subsequent heat treatment were analyzed (**Figure 3**). These catalysts were denoted as Fe@Co-X (X represents the applied potential during electrochemical reconstruction). Figure 3a shows the Raman spectra of the as-prepared electrodes. Both Fe@Co and Fe@Co-0.9 exhibit peaks at ≈470, 540, 590, and 700 cm^{-1}, which correspond to OCoO (E_g), CoO(F_{2g}), $Co(OH)_2$ (A_{1g}), and CoO (A_{1g}), respectively.[32,34,36] The peaks related to the Co^{2+} phase are mainly observed owing to the insufficient electrochemical oxidation of Co. Conversely, in the case of the Fe@Co-1.5 and Fc@Co-1.65 electrodes, the OCoO (E_g) and CoOOH (A_{1g}) peaks are predominant, suggesting the occurrence of structural reconstruction. The NF and Fe electrodes were also analyzed, verifying the distinct separation of Ni and Fe peaks from the Co peaks (Figure S8, Supporting Information). Figure 3b presents a comparison of the C_{dl} values of the electrodes measured in the non-Faradaic potential range (Figure S9, Supporting Information). The C_{dl} values of Fe@Co-0.9 (2.1 mF cm^{-2}), Fe@Co-1.5 (2.4 mF cm^{-2}), and Fe@Co-1.65 (2.2 mF cm^{-2}) are all greater than that of Fe@Co (1.8 mF cm^{-2}). This result indicates that the electrochemical treatment led to an enlargement of the ECSA and reached an optimal point at a specific potential. The observed increase in ECSA can be ascribed to an irreversible electrochemical reconstruction because the C_{dl} measurements were conducted within a potential range lower than 0.8 V (versus RHE), where the Co^{2+} phase is predominant. During the CV measurements, Fe@Co displayed an initial irreversible oxidation of Co in the first cycle, followed by a stable behavior in subsequent cycles (Figure S10, Supporting Information). The SEM images revealed alterations in the catalyst morphology due to electrochemical reconstruction. In the Fe@Co catalyst, Co-based particles with a size of hundreds of nanometers were observed (Figure 3c). As can be seen in Figure 3d, these particles underwent partial aggregation after electrochemical treatment at 0.9 V (versus RHE). In the Fe@Co-1.5 catalyst, Co-based nanosheet structures were apparent and gave rise to smaller particles compared to Fe@Co (Figure 3e). In the Fe@Co-1.65 catalyst, where the OER actively occurred, the Co-based nanosheet structure remained discernible but was partially obscured by a cracked layer (Figure 3f). EDS mapping

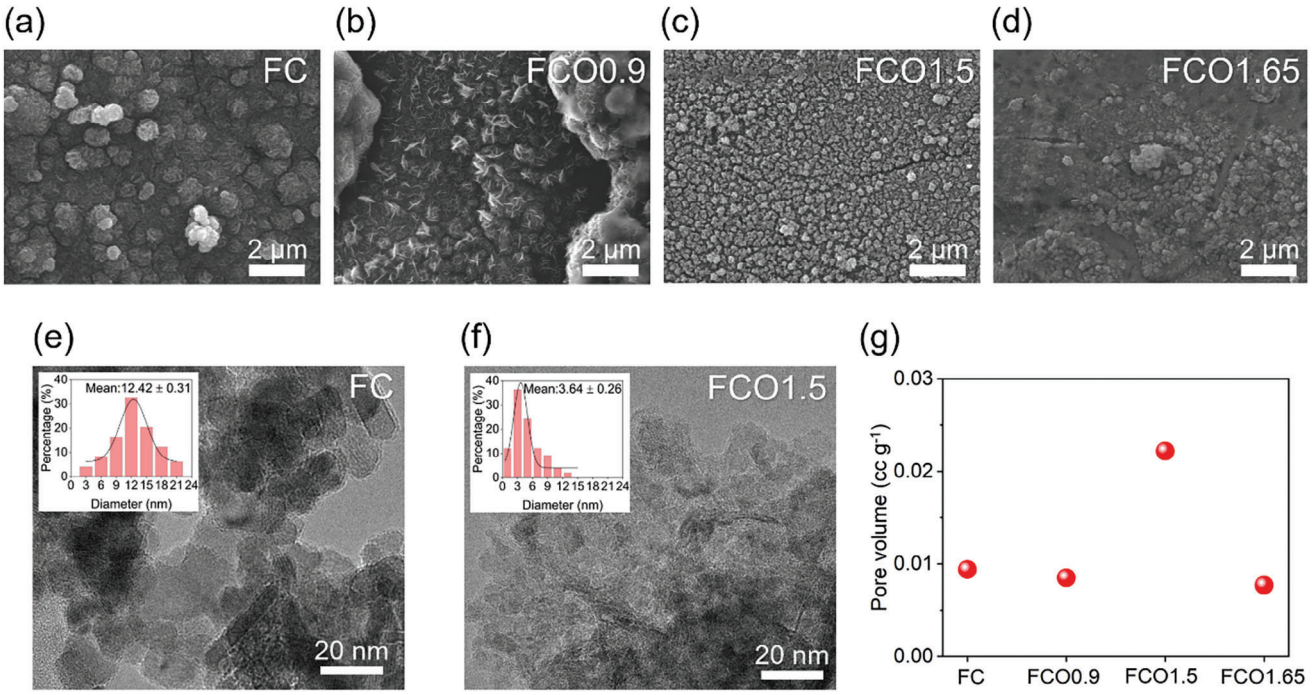

Figure 4. Material properties of the FC-electrode series. SEM images of a) FC, b) FCO0.9, c) FCO1.5, and d) FCO1.65 electrodes. TEM images of e) FC and f) FCO1.5 catalysts with the corresponding particle size distribution (inset). g) Pore volume of the electrodes measured with a porosimeter.

data indicated that this layer primarily comprised O, C, and Co (Figure S11 and Table S3, Supporting Information). In summary, in the Fe@Co catalyst, electrochemical reconstruction at a potential of 1.5 V (versus RHE) caused the oxidation of Co into CoOOH and CoO_2, resulting in a reduction in the particle size and an increase in the ECSA.

2.4. Characteristics of the Co-Based Catalysts after Heat Treatment

Next, the characteristics of the catalysts subjected to heat treatment were examined. As shown in **Figure 4**, the material properties of the heat-treated catalysts were analyzed via SEM, TEM, and porosimetry analyses to identify the extrinsic properties of the Co-based catalysts. The SEM image of the FC catalyst revealed a uniform distribution of submicron-sized Co-based particles (Figure 4a). In FCO0.9, the particles were partially agglomerated (Figure 4b). Conversely, FCO1.5 and FCO1.65 exhibited uniform distribution of particles in the tens-of-nanometer range, and FCO1.65 was prominently covered by a cracked layer (Figure 4c,d). Similar to Fe@Co-1.65, EDS mapping data indicated that this layer primarily comprised O, C, and Co (Figure S12 and Table S3, Supporting Information). The TEM images further revealed that FCO1.5 contained smaller particles (3.6 nm; Figure 4f) compared with FC (12.4 nm; Figure 4e). Additionally, the pore volume of each catalyst was determined using a mercury porosimeter (Figure 4g; Figure S13, Supporting Information). Notably, FCO1.5 exhibited a pore volume of ≈0.02 cc g^{-1}, which was approximately twice that of the other catalysts. This result is consistent with the ECSA trend depicted in Figure 2e. The elevated pore volume and ECSA of FCO1.5 can be elucidated in two ways. First, the increased ECSA and pore volume of FCO1.5 can be attributed to its particles being approximately one-third smaller than those of FC and FCO0.9. This result indicates that the electrochemical oxidation prior to heat treatment reduced the particle size and enhanced the ECSA of the catalysts. Second, the comparison between FCO1.5 and FCO1.65 revealed that the formation of an oxide layer due to the OER induced a reduction in the ECSA. This phenomenon was confirmed both before (Figure 3b) and after (Figure 2e) the heat treatment of the catalysts. Thus, an optimal electrochemical reconstruction potential exists concerning the extrinsic performance of the Co-based catalysts.

Figure 5 displays the results of in-situ Raman spectroscopy and X-ray photoelectron spectroscopy (XPS), which were conducted to examine the intrinsic properties of the Co-based catalysts. Figure 5a shows a structural change in FC according to the applied potential. The Raman spectra of FC at 0.9 V (versus RHE) showed three peaks ≈490, 530, and 700 cm^{-1}, which correspond to Co_3O_4 (E_g), Co_3O_4 (F_{2g}), and Co_3O_4 (A_{1g}), respectively.[26,52] Upon reaching a potential of 1.2 V (versus RHE), Co underwent a structural change, which led to a notable prominence of the OCoO (Eg) and CoO (F_{2g}) peaks. A similar result was observed for the FCO0.9 catalyst (Figure S14a, Supporting Information). Conversely, the Raman spectra of FCO1.5 showed a broad peak at ≈570 cm^{-1} at a potential of 0.9 V (versus RHE) (Figure 5b), which segregated into CoO (F_{2g}) and CoOOH (A_{1g}) peaks at a potential of 1.1 V (versus RHE). At a potential of 1.5 V (versus RHE), where the OER occurred, the CoOOH (A_{1g}) peak was observed along with the OCoO (E_g) peak. This phenomenon was also observed for FCO1.65 (Figure S14b, Supporting

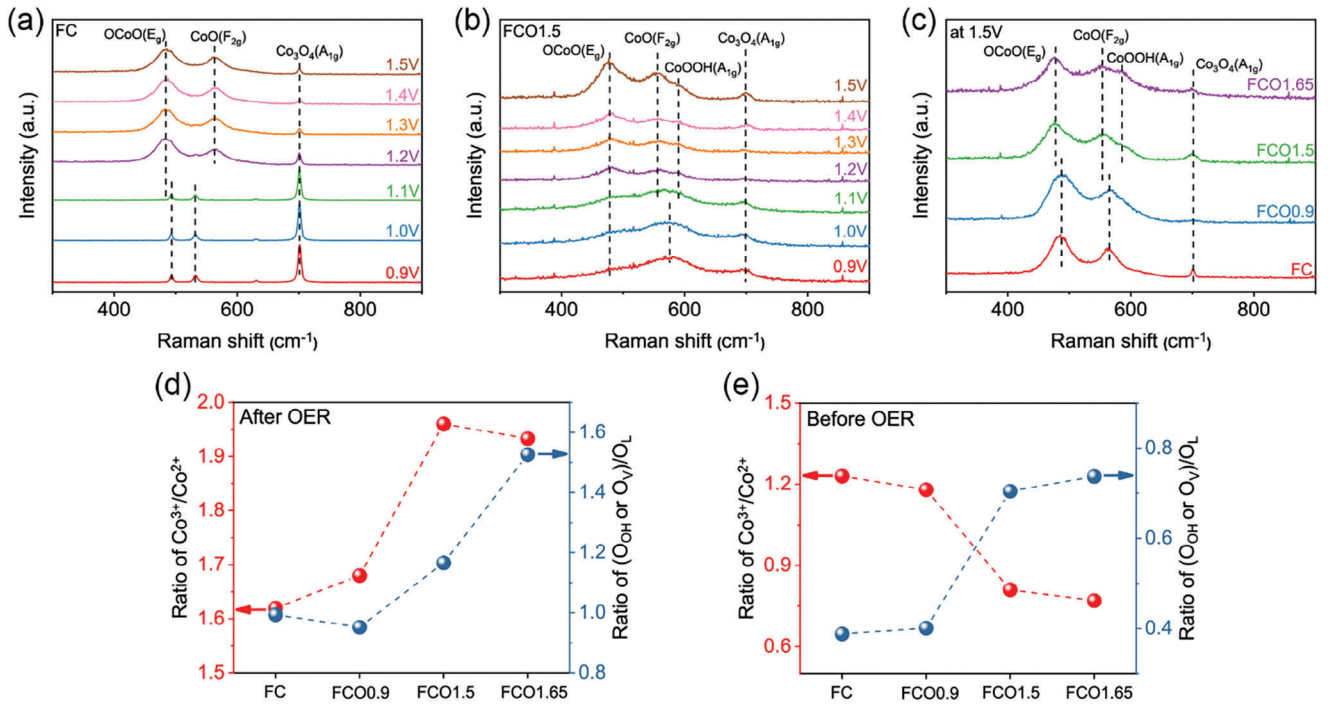

Figure 5. Electronic structure and properties of the FC-catalyst series. In-situ Raman spectra of the a) FC and b) FCO1.5 catalysts at applied potentials ranging from 0.9 to 1.5 V (versus RHE). c) Raman spectra of the as-prepared catalysts at 1.5 V (versus RHE). Comparison of the Co^{3+}/Co^{2+} and (O_{OH} or O_V)/O_L ratios of the electrodes d) after and e) before OER operation, which were measured via XPS analysis. The dashed lines were drawn to guide the eye.

Information). The structures during the OER can be clearly compared in Figure 5c, which displays the peaks of the catalysts at an applied potential of 1.5 V (versus RHE). FC and FCO0.9 exhibited similar structures, showing OCoO (E_g) and CoO (F_{2g}) peaks at ≈480 and 560 cm^{-1}, respectively. Conversely, in the Raman spectra of FCO1.5 and FCO1.65, these peaks redshifted by ≈8 cm^{-1} and were accompanied by a distinct CoOOH (A_{1g}) peak. These results, in conjunction with the CV findings (Figure 2d), indicate the persistence of the CoOOH phase during the OER in the FCO1.5 and FCO1.65 catalysts in contrast to the FC catalyst. Given that CoOOH is a well-established active site for Co,[26,29,32,36,50] the superior OER performance of FCO1.5 compared with that of FC can be ascribed to the retention of the CoOOH phase during the OER. The XPS analysis further validated the disparity in the oxidation states of Co in the prepared catalysts. Figure 5d depicts the post-OER XPS results, revealing higher Co^{3+}/Co^{2+} and (O_{OH} or O_V)/O_L (O_{OH} = hydroxyl, O_V = oxygen vacancy, and O_L = lattice oxygen) values for FCO1.5 compared with those for FC (Figure S15, see details in Supporting Information).[53,54] Because the O_L peak represents oxygen–metal bonding and the O_{OH} peak corresponds to a hydroxide,[9,42] structures such as Co_3O_4 or CoO_2 exhibit a lower O_{OH}/O_L value than CoOOH. Thus, the higher Co^{3+}/Co^{2+} and (O_{OH} or O_V)/O_L values for FCO1.5 compared with those for FC can be attributed to a substantial generation of CoOOH. Furthermore, FCO1.65 exhibited a lower Co^{3+}/Co^{2+} ratio than FCO1.5, indicating that excessive OER process before heat treatment impeded CoOOH formation. To elucidate the origin of the change in the oxidation states of the catalysts after OER, the catalysts were subjected to XPS analyses prior to the OER process (Figure S16, Supporting Information). As shown in Figure 5e, FCO1.5 and FCO1.65 exhibited higher proportions of (O_{OH} or O_V) and Co^{2+} than FC before OER. Ex-situ Raman spectra also confirmed that, before OER, FCO1.5 and FCO1.65 displayed pronounced $Co(OH)_2$ (E_g) peaks and relatively small Co_3O_4 peaks, whereas FC only exhibited peaks related to the Co_3O_4 structure (Figure S17, Supporting Information). In addition, electron paramagnetic resonance (EPR) analysis was performed to compare O_V concentrations between catalysts. Both FC and FCO1.5 showed an EPR signal centered at g = 2.004; however, the higher signal strength observed in FCO1.5 suggests a notable presence of O_V (Figure S18, Supporting Information).[55,56] Hence, within the Co_3O_4 spinel structure, FCO1.5 showed high concentrations of O_{OH} and O_V, resulting in a higher ratio of Co^{2+} compared to FC. Consequently, during the OER, FCO1.5 underwent oxidation to the Co^{3+} phase, forming CoOOH. Conversely, FC initially possessed a substantial Co^{3+} content, leading to the prevalence of Co^{4+} throughout the OER process. These variances in structure arose from the electrochemical oxidation preceding heat treatment. For the Fe@Co catalyst, initially structured with $Co(OH)_2$, the heat treatment instigated its transition into a Co_3O_4 spinel structure while concurrently raising the oxidation state of Co ions. However, in Fe@Co-1.5, where the CoOOH and CoO_2 phases were formed due to the electrochemical oxidation, when a change to a spinel structure occurs through subsequent heat treatment, Co ions undergo reduction, leading to the generation of O_V and a consequent lower oxidation state of Co compared to FC.[55] Since FCO1.5 is a multi-component catalyst, the roles of Fe and Ni

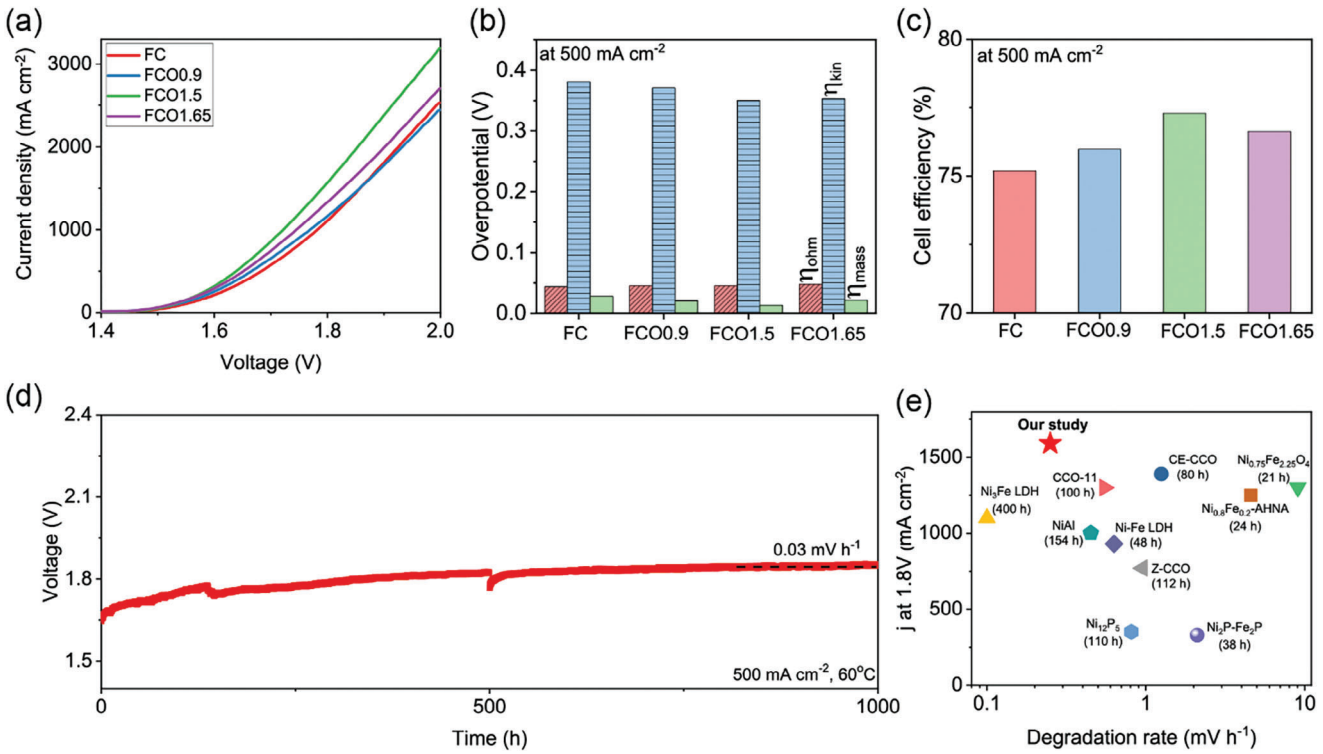

Figure 6. Water-splitting performance of the FC-catalyst series in the AEMWE single-cell systems. a) Polarization curves of the AEMWE systems. b) Comparison of the ohmic (η_{ohm}), kinetic (η_{kin}), and mass-transfer (η_{mass}) overpotentials of the AEMWE systems at a current density of 500 mA cm^{-2}. c) Single-cell efficiency of the AEMWE systems at 500 mA cm^{-2}. d) Durability test of the FCO1.5 AEMWE system at 500 mA cm^{-2} for 1000 h. e) Comparison of the performance and degradation rates of state-of-the-art AEMWE systems using transition metal–based anodes.[4,5,9,41,42,57–61].

were summarized (Figure S19,S20, and Table S4, Supporting Information), and it was confirmed that the performance difference between FC-series catalysts was mainly due to the structure change of Co. In summary, the changes in the catalyst behavior concerning OER activity resulting from electrochemical surface reconstruction can be categorized into extrinsic and intrinsic properties. Analysis of the extrinsic properties revealed that FCO1.5 comprised particles approximately three times smaller than FC, leading to enhanced ECSA and porosity. For the intrinsic features, FCO1.5 possessed higher concentrations of Co^{2+}, O_V, and O_{OH} than FC in the initial state, resulting in the effective preservation of the CoOOH phase during the OER.

2.5. AEMWE Single-Cell Measurements

To ascertain the practical water-electrolysis capacity of the prepared catalysts, their performance was evaluated in AEMWE single-cell systems. **Figure** 6a illustrates the polarization curves for each system, revealing that the water-splitting performance of FCO1.5 was superior to that of the other systems. At a cell voltage of 1.8 V, FCO1.5 achieved a current density of ≈1590 mA cm^{-2}, which represents a performance enhancement of ≈1.4-fold compared with FC (1120 mA cm^{-2}). For a comprehensive analysis of the cell performance, the total overpotential at 500 mA cm^{-2} was divided into ohmic (η_{ohm}), kinetic (η_{kin}), and mass-transfer (η_{mass}) overpotentials (Figure 6b), which were determined using electrochemical impedance spectroscopy (EIS), the Tafel slopes, and the deviation of the polarization curve from the Tafel slope, respectively (Figure S21,S22, Supporting Information).[42,62] All systems exhibited a similar η_{ohm} value of ≈0.045 V, while the FCO1.5 and FCO1.65 systems showed lower η_{kin} values (0.35 and 0.353 V, respectively) than the FC system (0.381 V) (Table S5, Supporting Information). The lower η_{kin} value in the FCO1.5 AEMWE system can be attributed to the preservation of the active CoOOH phase, as confirmed via the electrochemical and material analyses. FCO1.5 exhibited the lowest η_{mass} value of 0.013 V, which can be attributed to its smaller particle size and increased porosity compared with those of the other catalysts. The energy conversion efficiency at 500 mA cm^{-2} was calculated (Figure 6c). The cell efficiency of the FCO1.5 system reached ≈77.3%, representing a 2.1% increase compared with that of the FC system (75.2%). The single-cell stability was evaluated by subjecting the FCO1.5 AEMWE system to galvanostatic testing at 500 mA cm^{-2} for 1000 h at 60 °C (Figure 6d). Notably, FCO1.5 displayed a degradation rate of 0.2 mV h^{-1} after 1000 h of operation. Moreover, in the final 200 h of operation, the degradation rate was ≈0.03 mV h^{-1}, demonstrating an increased stability over time. The FCO1.5 catalyst exhibited superior performance and durability compared with state-of-the-art transition metal–based anodes (Figure 6e).[4,5,9,41,42,57–61] For an effective comparison of the catalyst performance in the AEMWE system, our system was compared with studies using commercial AEMs and ionomers under analogous conditions (1 M KOH, <65 °C, and >300 mA cm^{-2}). Furthermore, the water–gas displacement method was used to quantify the produced O_2, with the Faradaic efficiency

consistently exceeding 98% after 1000 h of operation (Figure S23, Supporting Information). Collectively, these findings demonstrate the promising potential of FCO1.5 for prospective AEMWE applications.

3. Conclusion

We developed a Co-based catalyst with exceptional OER performance and durability via a simple and scalable surface reconstruction strategy. Our study unveiled that electrochemical reconstruction followed by heat treatment significantly enhanced the OER performance of the Co-based catalysts. The FCO1.5 catalyst synthesized under optimal conditions demonstrated an increased ECSA and porosity owing to the formation of smaller particles compared with the FC catalyst. Moreover, the CoOOH phase was effectively maintained in FCO1.5 during the OER, as confirmed via in-situ Raman spectroscopy, leading to improved OER performance. Consequently, the FCO1.5 anode demonstrated an overpotential of 190 mV at 10 mA cm^{-2} and a Tafel slope of 32.7 mV dec^{-1} under half-cell conditions. In the AEMWE single-cell system, FCO1.5 showcased a current density of 1590 mA cm^{-2} at 1.8 V and 60 °C, and a degradation rate of 0.2 mV h^{-1} after 1000 h of operation at 500 mA cm^{-2}. This study provides a universally applicable strategy for enhancing catalytic OER activity and new insights into the mechanism underlying the enhancement of OER performance.

4. Experimental Section

Materials: $CoCl_2$ (99.995%), $FeCl_3$ (99.9%), $NiCl_2$ (99.9%), KOH (90%), and ethanol (99.9%) were purchased from Sigma-Aldrich Co. All solutions were prepared using deionized water (18.2 MΩ cm, Milli-Q Direct 8 system, Merck Millipore, MA, USA).

Synthesis of Anode Catalysts: First, the catalyst was synthesized via sequential electrodeposition of Fe and Co[3] on NF (thickness = 250 µm thickness, porosity = 60% porosity, and fiber diameter = 20 µm; 2Ni18-025, Bekaert), which was used as a substrate. The electrodeposition was conducted using a conventional three-electrode electrochemical cell, with NF, platinum foil, and a saturated calomel electrode (SCE) serving as the working, counter, and reference electrodes, respectively. NF was electrodeposited with Fe at −0.9 V (versus SCE) in a 50 mM $FeCl_3$ solution for 15 min. After a water rinse, the electrodes were dried at 40 °C for 20 min. Subsequently, the prepared electrode was electrodeposited with Co for 5 min at −0.95 V (versus SCE) in a 50 mM $CoCl_2$ solution, rinsed with water, and dried at 40 °C for 20 min. Next, the electrodeposited electrode was activated under constant potential conditions (0.9, 1.5, or 1.65 V versus RHE) in a 1 M KOH solution for 10 min. Afterward, the electrode was dried at 40 °C for 20 min and heat-treated at 400 °C for 1 h. The as-prepared electrodes were denoted as FCO0.9, FCO1.5, and FCO1.65 according to the applied potential during the electrochemical reconstruction stage. NF was also subjected to heat treatment at 400 °C for 1 h to serve as a control group. For preparing single-electrodeposited Co, Fe, and Ni electrodes, NF was electrodeposited with Co, Fe, and Ni in 50 mM $CoCl_2$, $FeCl_3$, and $NiCl_2$ solutions at −0.95, −0.9, and −0.95 V (versus SCE) for 5 min, respectively. Subsequently, the electrodes were operated at 1.5 V (versus RHE) in a 1 M KOH solution for 10 min. Afterward, the electrodes were dried at 40 °C for 20 min and heat-treated at 400 °C for 1 h.

Material Characterization: The crystal structure was analyzed via XRD analysis using a SmartLab (Rigaku, Japan) system with Cu Kα radiation (40 kV, 250 mA) in the 2θ range of 10°–70° at a scan speed of 3°s^{-1}. The surface morphology and elemental composition were determined via SEM-EDS using a JSM-7800F Prime microscope (JEOL, Japan) operating at an accelerating voltage of 15 kV. TEM and EDS analyses were performed at 200 kV using a JEM-F200 (JEOL, Japan). XPS was conducted using a K-alpha system (ThermoFisher Scientific, USA) equipped with an Al Kα µ-focused monochromator operating at 1486.6 eV. Raman spectra were obtained using a confocal Raman microscope (HEDA, NOST, Republic of Korea) with a 532-nm light source at applied potentials ranging from 0.9 to 1.5 V (versus RHE). For the in situ analysis, a Pt foil and SCE were used as the counter and reference electrodes, respectively. For reproducibility, each measurement was performed at least thrice. Each spectrum was calibrated using the silicon Raman peak at 520 cm^{-1}. The loading amount of the catalyst was measured via ICP-MS (NexION 2000, USA). The pore volume of the electrode was analyzed using a PM33GT porosimeter (Quantachrome, USA). The ESR analysis was conducted by an EMXplus-9.5/12/P/L system (Bruker, USA). For the ESR analysis, the FCO1.5 and FC catalysts were fabricated on carbon paper.

Electrochemical Measurements: The electrochemical tests were conducted using an SP-150 (Biologic, France) potentiostat with an SCE and Pt foil as the reference and counter electrodes, respectively. The potential of the SCE was calibrated by performing CV tests using $[Fe(CN)_6]^{4-}/[Fe(CN)_6]^{3-}$ before and after the electrochemical experiments. The OER activity was measured using LSV at a scan rate of 5 mV s^{-1} in a 1 M KOH solution. For the Tafel analysis, various current densities (1, 2, 5, 10, 20, 50, and 100 mA cm^{-2}) were applied for at least 3 min and the potentials that reached the steady-state were measured. To determine the ECSA of the catalysts, CV measurements were performed at 0.75–0.85 V (versus RHE) using scan rates of 20, 40, 60, 80, and 100 mV s^{-1}. The associated capacitance values were determined using the gradient of the linear correlation between the current density and scan rate. All electrochemical data were iR-compensated according to the ohmic resistance unless otherwise specified. The ohmic resistance was measured via EIS from 10 KHz to 1 Hz at an amplitude of 10 mV.

AEMWE Single-Cell Preparation and Measurement: For the AEMWE single-cell test, a Pt/C cathode and FC-based anode (1 cm^2) were used. Au-coated Ti flow fields and end plates were supplied by CNL Energy company. The Pt/C electrode was prepared using the spraying-coating method with a loading amount of 1 mg cm^{-2} on carbon paper (10 BC, Sigracet). A cathode ink slurry containing commercial Pt/C powder (47 wt.%, Tanaka K.K), 20 wt.% XB-7 ionomer (Dioxide Materials), water, and isopropyl alcohol was sonicated for 1 h before spray coating. For AEM, an X37-50 Grade RT membrane (Dioxide Materials) was used, which was immersed in 1 M KOH for 24 h before usage. In the AEMWE single-cell system, a 1 M KOH solution was supplied to the cathode and anode with a flow rate of 30 mL min^{-1} at 60 °C. The water-splitting performance was determined by measuring the LSV curves, which were obtained in the range of 1.35 to 2.0 V using a scan rate of 5 mV s^{-1}. For the durability test, the single-cell system was operated at a constant current density of 500 mA cm^{-2} for 1000 h. EIS measurements were performed at a cell voltage of 1.6 V from 10 KHz to 1 Hz at an amplitude of 10 mV. The cell efficiency was determined using Equation 1:

$$\text{Cell efficiency} = \frac{H_2 \text{ power out}}{\text{AEM electrolyzer power}} \times 100\% \quad (1)$$

The AEM electrolyzer power was calculated by multiplying the measured cell voltage and a current density of 500 mA cm^{-2}. The lower heating value was used as a measure for the H_2 power output. For the Faradaic efficiency analysis, the volume of the generated O_2 was measured using the water–gas displacement method at a current density of 500 mA cm^{-2} and compared with the theoretically calculated volume.[22] The Faradaic efficiency was determined using Equation 2:

$$\text{Faradaic efficiency} = \frac{nF \times m}{Q} \quad (2)$$

where n represents the number of electrons involved in generating one O_2 molecule ($n = 4$), F represents the Faraday constant (96 485 C mol^{-1}), m represents the amount of produced O_2 in moles, and Q represents the total charge passed.

Supporting Information

Supporting Information is available from the Wiley Online Library or from the author.

Acknowledgements

This work was supported by the National Research Foundation of Korea (NRF-2022R1A2C1091933 and NRF-2018R1A5A1024127).

Conflict of Interest

The authors declare no conflict of interest.

Data Availability Statement

The data that support the findings of this study are available in the supplementary material of this article.

Keywords

anion exchange membrane water electrolysis, cobalt, electrocatalysts, oxygen evolution reaction, surface reconstruction

Received: November 19, 2023
Revised: December 19, 2023
Published online: January 29, 2024

[1] N. Du, C. Roy, R. Peach, M. Turnbull, S. Thiele, C. Bock, *Chem. Rev.* **2022**.
[2] C. Santoro, A. Lavacchi, P. Mustarelli, V. Di Noto, L. Elbaz, D. R. Dekel, F. Jaouen, *ChemSusChem* **2022**, 202200027.
[3] S. Han, H. S. Park, J. Yoon, *Chem. Eng. J.* **2023**, *477*, 146713.
[4] W. Lee, H. Yun, Y. Kim, S. S. Jeon, H. T. Chung, B. Han, H. Lee, *ACS Catal.* **2023**.
[5] W. Jiang, A. Y. Faid, B. F. Gomes, I. Galkina, L. Xia, C. M. S. Lobo, M. Desmau, P. Borowski, H. Hartmann, A. Maljusch, A. Besmehn, C. Roth, S. Sunde, W. Lehnert, M. Shviro, *Adv. Funct. Mater.* **2022**, *32*.
[6] N. Chen, S. Y. Paek, J. Y. Lee, J. H. Park, S. Y. Lee, Y. M. Lee, *Energy Environ. Sci.* **2021**, *14*, 6338.
[7] B. Mayerhöfer, F. D. Speck, M. Hegelheimer, M. Bierling, A. Hafez, D. Dunia McLaughlin, S. Cherevko, S. Thiele, R. Peach, *J. Mater. Chem. A* **2021**.
[8] P. Chen, X. Hu, *Adv. Energy Mater.* **2020**, *10*, 1.
[9] M. J. Jang, J. Yang, J. Lee, Y. S. Park, J. Jeong, S. M. Park, J. Y. Jeong, Y. Yin, M. H. Seo, S. M. Choi, K. H. Lee, *J. Mater. Chem. A* **2020**, *8*, 4290.
[10] A. Meena, P. Thangavel, D. S. Jeong, A. N. Singh, A. Jana, H. Im, D. A. Nguyen, K. S. Kim, *Appl. Catal. B Environ.* **2022**, *306*, 121127.
[11] H. A. Miller, K. Bouzek, J. Hnat, S. Loos, C. I. Bernäcker, T. Weißgärber, L. Röntzsch, J. Meier-Haack, *Sustain. Energy Fuels* **2020**, *4*, 2114.
[12] I. Vincent, D. Bessarabov, *Renew. Sustain. Energy Rev.* **2018**, *81*, 1690.
[13] D. Li, E. J. Park, W. Zhu, Q. Shi, Y. Zhou, H. Tian, Y. Lin, A. Serov, B. Zulevi, E. D. Baca, C. Fujimoto, H. T. Chung, Y. S. Kim, *Nat. Energy* **2020**, *5*, 378.
[14] S. Zhao, L. Yan, H. Luo, W. Mustain, H. Xu, *Nano Energy* **2018**, *47*, 172.
[15] F. Razmjooei, T. Morawietz, E. Taghizadeh, E. Hadjixenophontos, L. Mues, M. Gerle, B. D. Wood, C. Harms, A. S. Gago, S. A. Ansar, K. A. Friedrich, *Joule* **2021**, *5*, 1776.
[16] R. R. Raja Sulaiman, W. Y. Wong, K. S. Loh, *Int. J. Energy Res.* **2021**, *1*.
[17] H. Jin, B. Ruqia, Y. Park, H. J. Kim, H. S. Oh, S. Il Choi, K. Lee, *Adv. Energy Mater.* **2021**, *11*, 1.
[18] D. Xu, M. B. Stevens, M. R. Cosby, S. Z. Oener, A. M. Smith, L. J. Enman, K. E. Ayers, C. B. Capuano, J. N. Renner, N. Danilovic, Y. Li, H. Wang, Q. Zhang, S. W. Boettcher, *ACS Catal.* **2019**, *9*, 7.
[19] H. Xia, Z. Huang, C. Lv, C. Zhang, *ACS Catal.* **2017**, *7*, 8205.
[20] J. Xiao, A. M. Oliveira, L. Wang, Y. Zhao, T. Wang, J. Wang, B. P. Setzler, Y. Yan, *ACS Catal.* **2021**, *11*, 264.
[21] J. Ping, Y. Wang, Q. Lu, B. Chen, J. Chen, Y. Huang, Q. Ma, C. Tan, J. Yang, X. Cao, Z. Wang, J. Wu, Y. Ying, H. Zhang, *Adv. Mater.* **2016**, *28*, 7640.
[22] P. Thangavel, M. Ha, S. Kumaraguru, A. Meena, A. N. Singh, A. M. Harzandi, K. S. Kim, *Energy Environ. Sci.* **2020**, *13*, 3447.
[23] F. Sun, L. Li, G. Wang, Y. Lin, *J. Mater. Chem. A* **2017**, *5*, 6849.
[24] M. A. Sayeed, T. Herd, A. P. O'Mullane, *J. Mater. Chem. A* **2016**, *4*, 991.
[25] Z. W. She, J. Kibsgaard, C. F. Dickens, I. Chorkendorff, J. K. Nørskov, T. F. Jaramillo, *Science (80-.)*. **2017**, *355*.
[26] Y. C. Liu, J. A. Koza, J. A. Switzer, *Electrochim. Acta* **2014**, *140*, 359.
[27] N. Jiang, B. You, M. Sheng, Y. Sun, *Angew. Chemie – Int. Ed.* **2015**, *54*, 6251.
[28] A. Bergmann, E. Martinez-Moreno, D. Teschner, P. Chernev, M. Gliech, J. F. De Araújo, T. Reier, H. Dau, P. Strasser, *Nat. Commun.* **2015**, *6*.
[29] M. S. Burke, M. G. Kast, L. Trotochaud, A. M. Smith, S. W. Boettcher, *J. Am. Chem. Soc.* **2015**, *137*, 3638.
[30] H. Xia, Z. Huang, C. Lv, C. Zhang, *ACS Catal.* **2017**, *7*, 8205.
[31] A. Bergmann, T. E. Jones, E. M. Moreno, D. Teschner, P. Chernev, M. Gliech, T. Reier, H. Dau, P. Strasser, *Nat. Catal.* **2018**, *1*, 711.
[32] A. Moysiadou, S. Lee, C. S. Hsu, H. M. Chen, X. Hu, *J. Am. Chem. Soc.* **2020**, *142*, 11901.
[33] F. T. Haase, A. Bergmann, T. E. Jones, J. Timoshenko, A. Herzog, H. S. Jeon, C. Rettenmaier, B. R. Cuenya, *Nat. Energy* **2022**, *7*, 765.
[34] W. H. Lee, M. H. Han, Y. J. Ko, B. K. Min, K. H. Chae, H. S. Oh, *Nat. Commun.* **2022**, *13*, 1.
[35] B. S. Yeo, A. T. Bell, *J. Am. Chem. Soc.* **2011**, *133*, 5587.
[36] W. Zheng, M. Liu, L. Y. S. Lee, *ACS Catal.* **2020**, *10*, 81.
[37] M. Zhang, M. De Respinis, H. Frei, *Nat. Chem.* **2014**, *6*, 362.
[38] J. Bai, J. Mei, T. Liao, Q. Sun, Z. G. Chen, Z. Sun, *Adv. Energy Mater.* **2022**, *12*, 1.
[39] W. Yang, C. Zhang, S. Du, B. Jiang, C. Wang, H. Bai, Z. Li, G. Huang, Y. Li, *Adv. Energy Mater.* **2022**, *12*, 1.
[40] P. Guo, J. Wu, X. B. Li, J. Luo, W. M. Lau, H. Liu, X. L. Sun, L. M. Liu, *Nano Energy* **2018**, *47*, 96.
[41] Y. Sei Park, Y. Park, M. Je Jang, J. Lee, C. Kim, M. Gyu Park, J. Yang, J. Choi, H. Mo Lee, S. Mook Choi, *Chem. Eng. J.* **2023**, *472*, 145150.
[42] Y. S. Park, J. Yang, J. Lee, M. J. Jang, J. Jeong, W. S. Choi, Y. Kim, Y. Yin, M. H. Seo, Z. Chen, S. M. Choi, *Appl. Catal. B Environ.* **2020**, *278*, 119276.
[43] E. López-Fernández, J. Gil-Rostra, C. Escudero, I. J. Villar-García, F. Yubero, A. de Lucas Consuegra, A. R. González-Elipe, *J. Power Sources* **2021**, *485*.
[44] X. Wu, K. Scott, *J. Mater. Chem.* **2011**, *21*, 12344.
[45] L. Wan, Z. Xu, P. Wang, P. F. Liu, Q. Xu, B. Wang, *Chem. Eng. J.* **2022**, *431*, 133942.
[46] T. Pandiarajan, L. J. Berchmans, S. Ravichandran, *RSC Adv.* **2015**, *5*, 34100.

[47] C. Liang, P. Zou, A. Nairan, Y. Zhang, J. Liu, K. Liu, S. Hu, F. Kang, H. J. Fan, C. Yang, *Energy Environ. Sci.* **2020**, *13*, 86.
[48] J. E. Park, M. J. Kim, M. S. Lim, S. Y. Kang, J. K. Kim, S. H. Oh, M. Her, Y. H. Cho, Y. E. Sung, *Appl. Catal. B Environ.* **2018**, *237*, 140.
[49] J. Chang, L. Liang, C. Li, M. Wang, J. Ge, C. Liu, W. Xing, *Green Chem.* **2016**, *18*, 2287.
[50] K. Ham, S. Hong, S. Kang, K. Cho, J. Lee, *ACS Energy Lett.* **2021**, *6*, 364.
[51] F. Wang, P. Zou, Y. Zhang, W. Pan, Y. Li, L. Liang, C. Chen, H. Liu, S. Zheng, *Nat. Commun.* **2023**, 1.
[52] L. Tian, J. L. Zhu, L. Chen, B. An, Q. Q. Liu, K. L. Huang, *J. Nanoparticle Res.* **2011**, *13*, 3483.
[53] H. Zhu, J. Zhang, R. Yanzhang, M. Du, Q. Wang, G. Gao, J. Wu, G. Wu, M. Zhang, B. Liu, J. Yao, X. Zhang, *Adv. Mater.* **2015**, *27*, 4752.
[54] S. Han, S. Kim, S. Kwak, C. Lee, D. H. Jeong, C. Kim, J. Yoon, *J. Ind. Eng. Chem.* **2022**, *108*, 514.
[55] K. Zhu, F. Shi, X. Zhu, W. Yang, *Nano Energy* **2020**, *73*, 104761.
[56] J. Hu, D. Jiang, Z. Weng, Y. Pan, Z. Li, H. Du, Y. Yuan, *Chem. Eng. J.* **2022**, *430*, 132736.
[57] J. Chang, Q. Lv, G. Li, J. Ge, C. Liu, W. Xing, *Appl. Catal. B Environ.* **2017**, *204*, 486.
[58] J. Lee, H. Jung, Y. Sei, S. Woo, N. Kwon, Y. Xing, S. Ho, S. Mook, J. Woo, B. Lim, *Chem. Eng. J.* **2021**, *420*, 127670.
[59] C. Liang, P. Zou, A. Nairan, Y. Zhang, J. Liu, K. Liu, S. Hu, F. Kang, H. J. Fan, C. Yang, *Energy Environ. Sci.* **2020**, *13*, 86.
[60] L. Wu, L. Yu, F. Zhang, B. McElhenny, D. Luo, A. Karim, S. Chen, Z. Ren, *Adv. Funct. Mater.* **2021**, *31*.
[61] L. Wang, T. Weissbach, R. Reissner, A. Ansar, A. S. Gago, S. Holdcroft, K. A. Friedrich, *ACS Appl. Energy Mater.* **2019**, *2*, 7903.
[62] L. Wan, Z. Xu, P. Wang, P. F. Liu, Q. Xu, B. Wang, *Chem. Eng. J.* **2022**, *431*, 133942.